# Computer simulations of the structure of colloidal ferrofluids

J. P. Huang*
*Max Planck Institute for Polymer Research, Ackermannweg 10, 55128 Mainz, Germany*

Z. W. Wang†
*Department of Chemistry, University of North Carolina at Chapel Hill, Chapel Hill, North Carolina 27599-3290, USA*

C. Holm‡
*Max Planck Institute for Polymer Research, Ackermannweg 10, 55128 Mainz, Germany*
(Received 13 August 2004; revised manuscript received 11 April 2005; published 30 June 2005)

The structure of a ferrofluid under the influence of an external magnetic field is expected to become anisotropic due to the alignment of the dipoles into the direction of the external field, and subsequently to the formation of particle chains due to the attractive head to tail orientations of the ferrofluid particles. Knowledge about the structure of a colloidal ferrofluid can be inferred from scattering data via the measurement of structure factors. We have used molecular-dynamics simulations to investigate the structure of both monodispersed and polydispersed ferrofluids. The results for the isotropic structure factor for monodispersed samples are similar to previous data by Camp and Patey that were obtained using an alternative Monte Carlo simulation technique, but in a different parameter region. Here we look in addition at bidispersed samples and compute the anisotropic structure factor by projecting the $q$ vector onto the $XY$ and $XZ$ planes separately, when the magnetic field was applied along the $z$ axis. We observe that the $XY$-plane structure factor as well as the pair distribution functions are quite different from those obtained for the $XZ$ plane. Further, the two-dimensional structure factor patterns are investigated for both monodispersed and bidispersed samples under different conditions. In addition, we look at the scaling exponents of structure factors. Our results should be of value to interpret scattering data on ferrofluids obtained under the influence of an external field.

DOI: 10.1103/PhysRevE.71.061203 PACS number(s): 61.20.Ja, 75.50.Mm, 82.70.Dd

## I. INTRODUCTION

Colloidal ferrofluids have received much attention over the past four decades due to their possible applications in various fields ranging from mechanical engineering [1] to biomedical employment (say, [2]). In fact, ferrofluids are colloidal suspensions containing single domain ferromagnetic particles distributed in a carrier liquid [3]. The structure of ferrofluids can be strongly influenced by external magnetic fields. The reason is that the single domain magnetic particles inside the ferrofluid can interact easily with the magnetic field, that in turn can affect the structural properties tremendously. Here, the particles interact with each other by the long-range anisotropic dipole-dipole potential as well as the short-range symmetric potentials, such as the steric repulsion, the electrostatic repulsion, and the Van der Waals attraction. Owing to these interactions, various microstructures have been experimentally found in ferrofluids [4–10]. In this connection, many theoretical and simulational works have focused on the understanding of the structural properties of ferrofluids. Interesting topics include the occurrence of the ferroelectric phase or spontaneous magnetization [11–18], the chain formation [15,19–36], and the gas-liquid phase transition behavior [23,37–44], etc. In particular, by using Monte Carlo techniques one [29] studied the formation of agglomerates in ferrofluids by taking into account the dependence on particle sizes, and found that the smallest particle size showed little evidence of ordering since thermal disordering dominates the situation. Also, a defect-induced two-phase coexistence was predicted [30] in dipolar fluids, namely, a dilute gas of chain ends coexisting with a high-density liquid of chain branching points. In addition, by using a Brownian dynamics calculation method [31], cluster structures and cluster aggregations were numerically investigated in a two-dimensional ferrofluid, too.

In practice, the structure of ferrofluids can be characterized by a pair distribution function [45]

$$g(\mathbf{r}) = \frac{V}{N^2}\left\langle \sum_i \sum_{j\neq i} \delta(\mathbf{r}-\mathbf{r}_{ij}) \right\rangle, \tag{1}$$

which is a function of the particle positions $\mathbf{r}$. Here $V$ denotes the volume of the sample, $N$ is the number of particles, and $\mathbf{r}_{ij}=\mathbf{r}_i-\mathbf{r}_j$ denotes the difference of the position vectors $\mathbf{r}_i$ and $\mathbf{r}_j$. The pair distribution function gives the probability of finding a pair of particles at a given distance $r=|\mathbf{r}|$ apart. Structure factors can be obtained from scattering experiments, which, however, are just related to the pair distribution functions by an inverse Fourier transform. The structure factor has been studied for isotropically dispersed ferrofluids

*Corresponding author. Electronic addresses: jphuang@mpip-mainz.mpg.de, jphuang@alumni.cuhk.net
†Electronic address: wangzw@email.unc.edu
‡Present address: FIAS, JW Goethe - Universität, Max-von-Laue Strasse 1, Frankfurt/Main, Germany. Electronic address: holm@mpip-mainz.mpg.de

 

where no external field is applied (say, [22]). In the case of an applied external field exerted on the system, anisotropy is expected to appear inside this system due to the formation of particle chains which get aligned in the direction of the external applied magnetic field [15,19–31]. In this case, the study of the anisotropic structure factor seems to be more appropriate, where the structure factor is projected onto a certain geometric plane [27,28,46–48] in order to get the information of the anisotropic structural properties of the model ferrofluid of interest. In other words, basic features of the anisotropy of the structure of the ferrofluids can be inferred by investigating the anisotropic structure factor (or pair distribution function), which can also be accessed experimentally [27,49].

Since all commercially available ferrofluids are polydispersed, we also discuss the structural property of a polydispersed system, which is different from that of a monodispersed system [10,26,50–53]. Bidispersed ferrofluids containing either dipolar particles with equal diameters and different dipole moments [54] or particles with different diameters and equal dipole moments have also been recently studied by means of density-functional theory. As a starting point, we therefore also investigate the physical properties of a bidispersed ferrofluid.

In the present paper, we analyze data obtained by a Langevin dynamics simulation method. These data have been obtained in earlier simulation of the equilibrium properties of monodispersed and bidispersed ferrofluids [25,26,55]. The long-range dipolar interactions are computed using the Ewald summation with the metallic boundary condition. In addition, we have also performed a check with a model monodispersed ferrofluid of $N=250$ and 2000 particles at the same density and a model bidispersed ferrofluid of $N=3029$ at the corresponding density, which all showed identical results to the corresponding 1000-particle system. Thus, without loss of generality, we shall investigate 1000 particles for the following simulations.

The paper is organized as follows. In Sec. II, we describe the molecular-dynamics simulations in use. In Sec. III, the simulation results are presented for the monodispersed and bidispersed cases, respectively. This is followed by a discussion and conclusions in Sec. IV.

## II. MOLECULAR DYNAMICS SIMULATIONS

### A. Langevin initial susceptibility

Let us start with a dilute monodispersed ferrofluid. In fact, the dilute ferrofluid can be considered as a gas consisting of noninteracting particles [56]. In this case, it is possible to write the equilibrium magnetization $M_L$ with the aid of the Langevin function $L(\alpha)=\coth(\alpha)-1/\alpha$, and one obtains

$$M_L = \frac{mN}{\mu_0 V} L(\alpha), \tag{2}$$

where $m$ stands for the magnetic moment of a particle and $\mu_0=4\pi\times10^{-7}$ H/m. Here $\alpha=mH/kT$ represents the Langevin parameter, where $H$ denotes the strength of the magnetic field, $k$ is the Boltzmann constant, and $T$ is the temperature. For this model, one can obtain the Langevin susceptibility, which has been demonstrated in Ref. [25],

$$\chi_L = \frac{4}{3}\pi\rho\lambda\sigma^3, \tag{3}$$

where $\lambda=m^2/4\pi\mu_0 kT\sigma^3$ represents the dipolar coupling constant, $\rho=N/V$ is the number density of the particles, and $\sigma$ is the diameter of the particle. However, in concentrated ferrofluids, the interparticle interaction is expected to play an important role, thus leading to a significant increase of the Langevin initial susceptibility $\chi_L$.

### B. Simulation method

The model system we study consists of a system composed of $N$ spherical particles of diameter $\sigma$ distributed in a cubic simulation box of side length $L$. Each particle has a permanent point dipole moment $\mathbf{m}_i$ which is located at its center. Then, the dipole-dipole interaction potential between particle $i$ and $j$ and all the images of $j$ is given by

$$U_{ij}^{DD} = \frac{1}{4\pi\mu_0} \times \sum_{\mathbf{n}} \left( \frac{\mathbf{m}_i\cdot\mathbf{m}_j}{|\mathbf{r}_{ij}+\mathbf{n}L|^3} - \frac{3[\mathbf{m}_i\cdot(\mathbf{r}_{ij}+\mathbf{n}L)][\mathbf{m}_j\cdot(\mathbf{r}_{ij}+\mathbf{n}L)]}{|\mathbf{r}_{ij}+\mathbf{n}L|^5} \right), \tag{4}$$

under the periodic boundary condition along all spatial directions. Here $\mathbf{r}_{ij}=\mathbf{r}_i-\mathbf{r}_j$ denotes the displacement vector of the two particles, and the sum extends over all simple cubic lattice points, $\mathbf{n}=(n_x,n_y,n_z)$ in a spherical summation order, where $n_x,n_y,n_z$ are integers. Our molecular-dynamics simulation method is the same as the one implemented in a previous paper [25].

We use the Ewald summation for dipolar systems to evaluate Eq. (4) effectively, which gives [45,57,58]

$$U_{ij}^{DD} = U_{ij}^{(R)} + U_{ij}^{(k)} + U_{ij}^{(S)} + U_{ij}^{(F)}, \tag{5}$$

where the real-space $U_{ij}^{(R)}$, the reciprocal-space $U_{ij}^{(K)}$, the self $U_{ij}^{(S)}$, and the surface $U_{ij}^{(F)}$ contributions are, respectively, given by

$$U_{ij}^{(R)} = \frac{1}{4\pi\mu_0}\sum_{\mathbf{n}\in\mathbb{Z}^3} \{(\mathbf{m}_i\cdot\mathbf{m}_j)R_1(|\mathbf{r}_{ij}+\mathbf{n}L|) - [\mathbf{m}_i\cdot(\mathbf{r}_{ij}+\mathbf{n}L)] \times [\mathbf{m}_j\cdot(\mathbf{r}_{ij}+\mathbf{n}L)]R_2(|\mathbf{r}_{ij}+\mathbf{n}L|)\}, \tag{6}$$

$$U_{ij}^{(K)} = \frac{1}{4\pi\mu_0 L^3}\sum_{\mathbf{k}\in\mathbb{Z}^3,\mathbf{k}\neq0} \frac{4\pi}{k^2} \times \exp[-(\pi k/\kappa L)^2](\mathbf{m}_i\cdot\mathbf{k})(\mathbf{m}_j\cdot\mathbf{k})\exp(2\pi i\mathbf{k}\cdot\mathbf{r}_{ij}/L), \tag{7}$$

$$U_{ij}^{(S)} = -\frac{1}{4\pi\mu_0}\frac{2\kappa^3}{3\sqrt{\pi}}(m_i^2+m_j^2), \tag{8}$$

$$U_{ij}^{(F)} = \frac{1}{4\pi\mu_0}\frac{4\pi}{(2\mu_{BC}+1)L^3}\mathbf{m}_i\cdot\mathbf{m}_j, \tag{9}$$

with $R_1(x)=[\mathrm{erfc}(\kappa x)+(2\kappa x/\sqrt{\pi})\exp(-\kappa^2x^2)]/x^3$ and $R_2(x)=[3\ \mathrm{erfc}(\kappa x)+(2\kappa x/\sqrt{\pi})(3+2\kappa^2x^2)\exp(-\kappa^2x^2)]/x^5$, where $\mathrm{erfc}(x)\equiv 2\pi^{-1/2}\int_x^\infty \exp(-t^2)\mathrm{d}t$ stands for the complementary error function, and the inverse length $\kappa$ denotes the splitting parameter of the Ewald summation. We take $\mu_{BC}=\infty$ (metallic boundary condition), which results in a vanishing surface term as well as a vanishing demagnetization field.

The steric interaction between two ferrofluid particles is modeled with a purely repulsive Lennard-Jones (LJ) potential of the form

$$U_{ij}^{\mathrm{LJ}} = 4\epsilon\left[\left(\frac{\sigma}{r_{ij}}\right)^{12}-\left(\frac{\sigma}{r_{ij}}\right)^{6}-O(R_c)\right], \tag{10}$$

where $O(R_c)=(\sigma/R_c)^{12}-(\sigma/R_c)^6$ with a cutoff radius $R_c=2^{1/6}\sigma$, meaning that $U_{ij}^{\mathrm{LJ}}=0$ for $r_{ij}\geqslant R_c$. The exact form of the soft sphere potential is irrelevant, and a simple $r^{-12}$ potential would have given similar results, representing the properties of a hard-sphere dipolar fluid that is often considered in analytical theories. However, we expect that using a full LJ potential, i.e., with a short-range attraction, will give slightly different results, since also the phase behavior is known to differ [39,42].

Similar to Ref. [25], a Langevin dynamics implementation is used to thermostat the system. The translational and rotational Langevin equations of motion of particle $i$ are given by

$$M_i\dot{\mathbf{v}}_i = \mathbf{F}_i - \Gamma_T\mathbf{v}_i + \boldsymbol{\xi}_i^T, \tag{11}$$

$$\mathbf{I}_i\cdot\dot{\boldsymbol{\omega}}_i = \boldsymbol{\tau}_i - \Gamma_R\Omega_i + \boldsymbol{\xi}_i^R, \tag{12}$$

where $M_i$ and $\mathbf{I}_i$ denotes the mass and inertial tensor of the particle, and $\Gamma_T$ and $\Gamma_R$ are the translational and rotational friction constants, respectively. Here the first moments of the Gaussian random force and torque should vanish, namely $\langle\xi_{i\alpha}^T(t)\rangle=0$ and $\langle\xi_{i\alpha}^R(t)\rangle=0$, whereas their second moments satisfy $\langle\xi_{i\alpha}^T(t)\xi_{j\beta}^T(t')\rangle=6kT\Gamma_T\delta_{ij}\delta_{\alpha\beta}\delta(t-t')$ and $\langle\xi_{i\alpha}^R(t)\xi_{j\beta}^R(t')\rangle=6kT\Gamma_R\delta_{ij}\delta_{\alpha\beta}\delta(t-t')$, where $\alpha$ and $\beta$ represent the $x,y,z$ components in the Cartesian coordinates, respectively.

In all simulations, we fixed the root mean square (rms) absolute errors in the dipolar forces to $\Delta F^{dip}\leqslant 10^{-4}m^2/4\pi\mu_0\sigma^4$, which corresponds to $10^{-4}/6$ of the attractive force between two contacting particles with dipole moments in parallel alignment. The optimal values of the Ewald parameters for this choice had been determined separately for each system using theoretical estimates [58]. This enabled us to minimize the overall computational time for a predefined accuracy. For the present simulations, the variables are given in dimensionless reduced form by the following units: length $r^*=r/\sigma$, dipole moment $m^{*2}=m^2/4\pi\mu_0\epsilon\sigma^3$, moment of inertia $I^*=I/M\sigma^2$ ($M$: mass of a particle), time $t^*=t(\epsilon/M\sigma^2)^{1/2}$, friction constants $\Gamma_T^*=\Gamma_T(\sigma^2/M\epsilon)^{1/2}$ and $\Gamma_R^*=\Gamma_R/(M\sigma^2\epsilon)^{1/2}$, and magnetic field $H^*=H(4\pi\mu_0\sigma^3/\epsilon)^{1/2}$, as well as temperature $T^*=kT/\epsilon$. The values of the dimensionless friction constants are used as $\Gamma_T^*=10.0$ and $\Gamma_R^*=3.0$, respectively. The orientational coordinates of the particles were expressed in terms of quaternion parameters, and the equations of motion were integrated via a leap-frog algorithm [45]. We set $I^*=0.4$ for the dimensionless moment of inertia, and performed the simulations at the constant temperature $T^*=1$ and the reduced time step $\Delta t^*=0.002$. By taking into account a monodispersed ferrofluid having magnetite particles with diameter $\sigma=10$ nm, we obtain the dipolar coupling constant $\lambda=1.3$ at room temperature $T=300$ K. In the case of larger particles with $\sigma=13$ nm (or 16 nm), we obtain $\lambda=2.9$ (or 5.32) under the same conditions. It is worth remarking that $\lambda$ may be further enlarged by decreasing the temperature or using cobalt as a working material. In the simulations, the runs were started from initial configurations with random particle positions and dipole moment orientations. For each case, the system was at first simulated for a period of at least 50 000 time steps, ensuring the equilibration of the magnetization. The structural properties were then calculated from the data for another period of at least 200 000 time steps. Next, the structural properties, i.e., structure factors and pair distribution functions, were calculated by sampling the system every 1000 time steps in the equilibrium state.

For the bidispersed system [26], the large magnetite particles had a diameter $\sigma_L=16$ nm and a dipolar coupling constant $\lambda_L=5.32$ (at $T=300$ K) and the small particles had $\sigma_S=10$ nm and $\lambda_S=1.3$ (at $T=300$ k), respectively. In view of the different sizes of the particles, the corresponding purely repulsive LJ potential representing the short-range interactions between the particles is given by

$$U_{ij}^{\mathrm{LJ}} = 4\epsilon\left[\left(\frac{\sigma_i+\sigma_j}{2r_{ij}}\right)^{12}-\left(\frac{\sigma_i+\sigma_j}{2r_{ij}}\right)^{6}\right]+\epsilon, \tag{13}$$

with a cutoff radius $R_c=2^{-5/6}(\sigma_i+\sigma_j)$. The other simulation parameters for the model bidispersed ferrofluid are the same as those for the above-mentioned monodispersed system, by replacing the physical parameters of a reference particle with those of a small particle, e.g., $\sigma\rightarrow\sigma_S$ and $M\rightarrow m_{a0}$. Here $m_{a0}$ denotes the mass of a small particle. In particular, for the large particles in the bidispersed system, the corresponding reduced variables in dimensionless form are as follows: dipole moment $m^{*2}=m^2/(4\pi\mu_0\epsilon\sigma_S^3)$, mass for the large particles $m_{b0}^*=m_{b0}/m_{a0}=(\sigma_L/\sigma_S)^3$, and moment of inertia $I^*=I/(m_{a0}\sigma_S^2)$. For more details of the simulation, please refer to Ref. [26]. The dipole moment of a large magnetite particle is given by $m=8.2\times10^{-19}$ A m$^2$ according to the dipole moment of a 10 nm particle $2\times10^{-19}$ A m$^2$ [10], the mass of the large particle is $m_{b0}=1.07\times10^{-20}$ Kg according to the bulk density of magnetite $5\times10^3$ Kg/m$^3$, and thus its moment of inertia is $I=2.74\times10^{-37}$ Kg m$^2$.

### C. Structure factor

Based on the simulation data, it is straightforward to calculate the structure factor [59], which is actually a Fourier transformation of the pair distribution function [Eq. (1)],

$$S(\mathbf{q}) = \frac{1}{N}\left\langle \left(\sum_{i=1}^{N} \cos \mathbf{q}\cdot\mathbf{r}_i\right)^2 + \left(\sum_{j=1}^{N} \sin \mathbf{q}\cdot\mathbf{r}_j\right)^2 \right\rangle. \quad (14)$$

The wave vectors $\mathbf{q}$ have to be commensurate with the periodic boundary conditions, i.e., $\mathbf{q}=(2\pi/L)(l,m,n)\neq(0,0,0)$, where $l$, $m$, and $n$ are integers. The precision of the structure factors is usually limited for small $q$; in this work, we take $2\pi/L \leqslant |\mathbf{q}| \leqslant 9$, where $2\pi/L$ is the smallest available value of $|\mathbf{q}|$ because of the size of the simulation box. This covers the $q$ region of interest, and a similar range was also studied in Ref. [28]. Since for the isotropic fluid the structure is rotationally invariant, $S(\mathbf{q})$ is obtained by averaging the contributions from all the wave vectors of magnitude $|\mathbf{q}|$. The anisotropic structure factor $S(q_{xy})$ [or $S(q_{xz})$] was obtained by omitting the $z$ (or $y$) component of $\mathbf{q}$ and $\mathbf{r}$ in Eq. (14) [46–48]. According to the general relation between $S(\mathbf{q})$ and $g(\mathbf{r})$ [59],

$$S(\mathbf{q}) = 1 + \rho \int [g(\mathbf{r}) - 1]e^{-i\mathbf{q}\cdot\mathbf{r}}\mathrm{d}\mathbf{r}, \quad (15)$$

there is a relation between $S(q_{xy})$ and the anisotropic pair distribution function $g(r_{xy})$,

$$S(q_{xy}) = 1 + \rho \int \mathrm{d}r_x \int \mathrm{d}r_y \int \mathrm{d}r_z [g(r_{xy}) - 1]e^{-i(q_x r_x + q_y r_y)}. \quad (16)$$

Accordingly, $S(q_{xz})$ possesses a similar expression. However, we computed our $S(q_{xy})$ and $S(q_{xz})$ by using Eq. (14), and not via the definition of the Fourier transform of the pair distribution function.

Anisotropic structure factors of ferrofluids were investigated, respectively, in experiments [27] and computer simulations [28]. To compare with the experimental results [27], an anisotropic structure factor was defined in the $(q_\perp, \theta', q_\parallel)$ cylindrical coordinates due to the cylindrical symmetry around the axis of an external applied magnetic field [28], in contrast to ours defined in the $(q_x, q_y, q_z)$ Cartesian coordinates. The relations are $q_\perp = \sqrt{q_x^2 + q_y^2}$ and $q_\parallel = q_z$, which were both used in Eq. (14) to compute the 2D structure factor $S(q_\perp, q_\parallel)$ shown in Figs. 6 and 10 (where the structure factor is projected onto the $q_\perp$ and $q_\parallel$ plane). This avoids using some smoothing functions, as has been done in Ref. [28], where according to Eq. (15), $S(q_\perp, q_\parallel)$ was computed from the pair distribution function $g(r_\perp, r_\parallel)$,

$$S(q_\perp, q_\parallel) = 1 + \rho \int_{-\infty}^{\infty} \mathrm{d}r_\parallel \int_0^{\infty} \mathrm{d}r_\perp \int_0^{2\pi} r_\perp \mathrm{d}\theta [g(r_\perp, r_\parallel) - 1] \times e^{-i(q_\perp r_\perp \cos\theta + q_\parallel r_\parallel)}, \quad (17)$$

with $r_\perp = \sqrt{r_x^2 + r_y^2}$ and $r_\parallel = r_z$. Owing to the different representation in use, our $S(q_{xy})$ is equivalent to the structure factor $S(\theta)$ at $\theta=90°$ or 270° [$S(\theta)$ denotes the structure factor $S(q)$ with $q = \sqrt{q_\perp^2 + q_\parallel^2}$ as a function of the angle $\theta$ between the wave vector $\mathbf{q}$ and the direction of field $\mathbf{H}$], as used in Figs. 5–8 in Ref. [28] or Figs. 3(a) and 8 in Ref. [27]. In this work, because of the isotropic behavior along the $x$ and $y$ axes, there should be $S(q_{xz}) = S(q_{yz}) = S(q_{\perp z})$, where $S(q_{\perp z})$ denotes the structure factor obtained from $S(q_{xz})$ [or $S(q_{yz})$] by replacing $q_x$ (or $q_y$) with $q_\perp$. In this regard, our $S(q_{xz})$ can be seen to be equivalent to the averaged structure factor $\bar{S}(\theta) = (1/360°)\int S(\theta)\mathrm{d}\theta$.

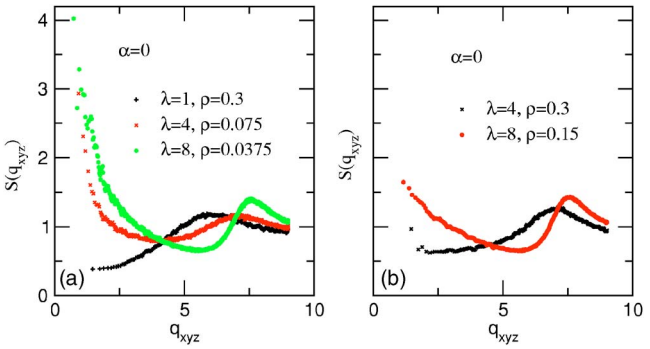


FIG. 1. (Color online) *Monodispersed case*: Structure factor $S(q_{xyz})$ for (a) $\chi_L = 0.4\pi$ and (b) $\chi_L = 1.6\pi$ as a function of λ at zero field ($\alpha=0$). It is worth noting that all the quantities plotted in Figs. 1–10 are dimensionless naturally [e.g., $S(q)$ and $g(r)$], or that they were already normalized to be dimensionless (e.g., $r$, $q$, $x$, and $y$) in the text.

## III. SIMULATION RESULTS

The results for the monodispersed ferrofluid are shown in Figs. 1–6. In Fig. 1, the isotropic structure factor $S(q_{xyz})$ is plotted for Langevin initial susceptibility (a) $\chi_L = 0.4\pi$ and

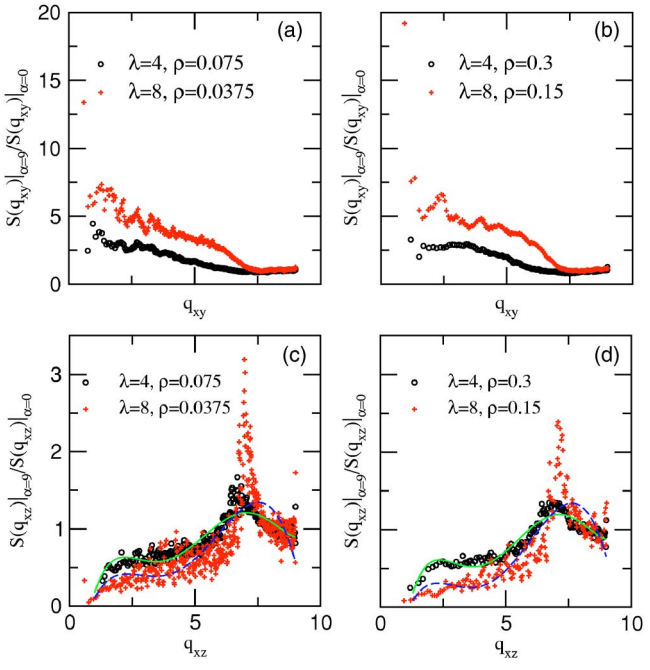


FIG. 2. (Color online) *Monodispersed case*: Ratio of the nonzero-field structure factor to the zero-field (a,b) $S(q_{xy})|_{\alpha=9}/S(q_{xy})|_{\alpha=0}$ and (c,d) $S(q_{xz})|_{\alpha=9}/S(q_{xz})|_{\alpha=0}$, for (a,c) $\chi_L = 0.4\pi$ and (b,d) $\chi_L = 1.6\pi$ as a function of λ. In (c,d), the solid (or long-dashed) line is a guide for the eye for λ=4 (or λ=8).

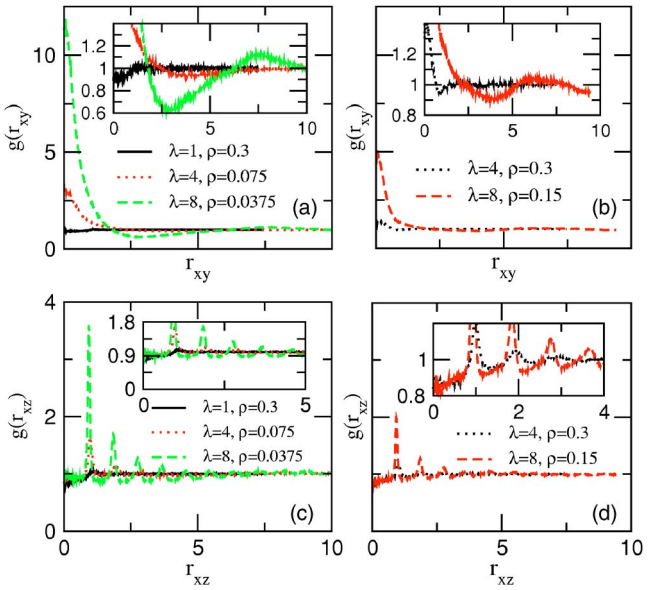


FIG. 3. (Color online) *Monodispersed case*: Pair distribution function (a,b) $g(r_{xy})$ and (c,d) $g(r_{xz})$ for (a,c) $\chi_L=0.4\pi$ and (b,d) $\chi_L=1.6\pi$ as a function of λ at nonzero field ($\alpha=9$). For clarity, the interesting parts of the figures are enlarged in the insets, respectively.

(b) $\chi_L=1.6\pi$ as a function of dipolar coupling constant λ at zero field ($\alpha=0$). It is found that high density can suppress the structure factor at the region of low $q$ vectors, for the same λ. As a matter of fact, this has also been found by Camp and Patey when they performed a Monte Carlo simulation of a dipolar system consisting of 256 particles [22] at $\lambda\approx 7.7$ at various densities. On the other hand, at given $\chi_L$, high-density $\rho$ (or low λ) can suppress again the structure factor at the region of low wave vectors. A result of classical statistical mechanics is that

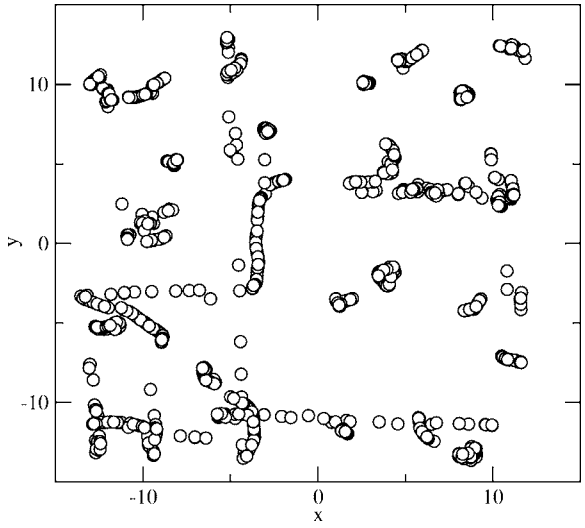


FIG. 4. Projection of particle locations onto the *XY* plane, to account for the depletion observed for λ=8 in Fig. 3(a).

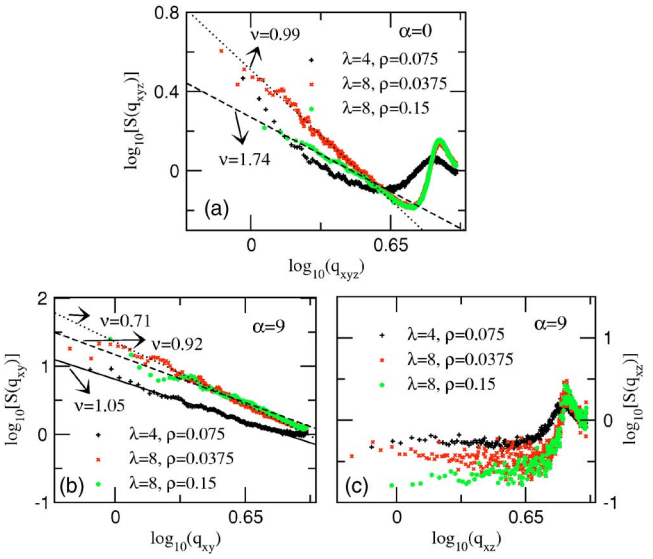


FIG. 5. (Color online) *Monodispersed case*: Log-log plots of the structure factors, (a) $S(q_{xyz})$, (b) $S(q_{xy})$, and (c) $S(q_{xz})$, for (a) zero field ($\alpha=0$) and (b,c) nonzero field ($\alpha=9$) as a function of λ and/or $\chi_L$. The curves denote the fitting: (a) dotted line for λ=8 and $\rho\sigma^3=0.0375$ ($\chi_L=0.4\pi$); dashed line for λ=8 and $\rho\sigma^3=0.15$ ($\chi_L=1.6\pi$); (b) solid line for λ=4 and $\rho\sigma^3=0.075$ ($\chi_L=0.4\pi$); dotted line for λ=8 and $\rho\sigma^3=0.0375$ ($\chi_L=0.4\pi$); dashed line for λ=8 and $\rho\sigma^3=0.15$ ($\chi_L=1.6\pi$). The corresponding scaling exponents $\nu$ are indicated in the figure.

$$S(q_{xyz}=0)=\eta_T/\eta_T^{\text{ideal}}, \tag{18}$$

where $\eta_T$ is the compressibility of the fluid, and $\eta_T^{\text{ideal}}=\beta/\rho$ is the compressibility of the ideal gas [59]. Thus $S(q_{xyz}=0)$ is a measure for the density fluctuations of the system. It is clear to see that the high density can reduce the compressibility of the ferrofluid, and hence in view of Eq. (18) $S(q_{xyz}=0)$ should be reduced accordingly, which just explains the present observation that increasing the density causes the structure factor of the low $q$ vectors $S(q_{xyz}\sim 0)$ to decrease.

At larger values of $q\approx 5$, we observe the occurrence of a peak that gets more pronounced for larger values of λ. This peak is due to short-range positional correlations. At small λ, there are only weak correlations, corresponding to the presence of small, loosely bound clusters. At higher values of λ, the peaks, and therefore the correlations, get more pronounced, and at λ=8 many particles are involved in clusters, leading to a sharp peak at real space distance $\sigma$. In addition, we also studied an intermediate coupling case of λ=6. As expected, the obtained structure factor lies between those for λ=8 and λ=4. Thus, for clarity, the result for the middle λ is not shown in the present paper. The isotropic structure factor shown in Fig. 1 can be compared with the experimental results [27]. In detail, Fig. 10 in Ref. [27] displays a zero-field isotropic structure factor for the sample A with volume fraction of particles $\phi=0.19$, which corresponds to number density $\rho=0.36$ and λ=1.75 in our notation. The framework of the structure factor is similar to that of Fig. 1(a) for λ=1 and $\rho=0.3$. That is, the structure factor begins from a value

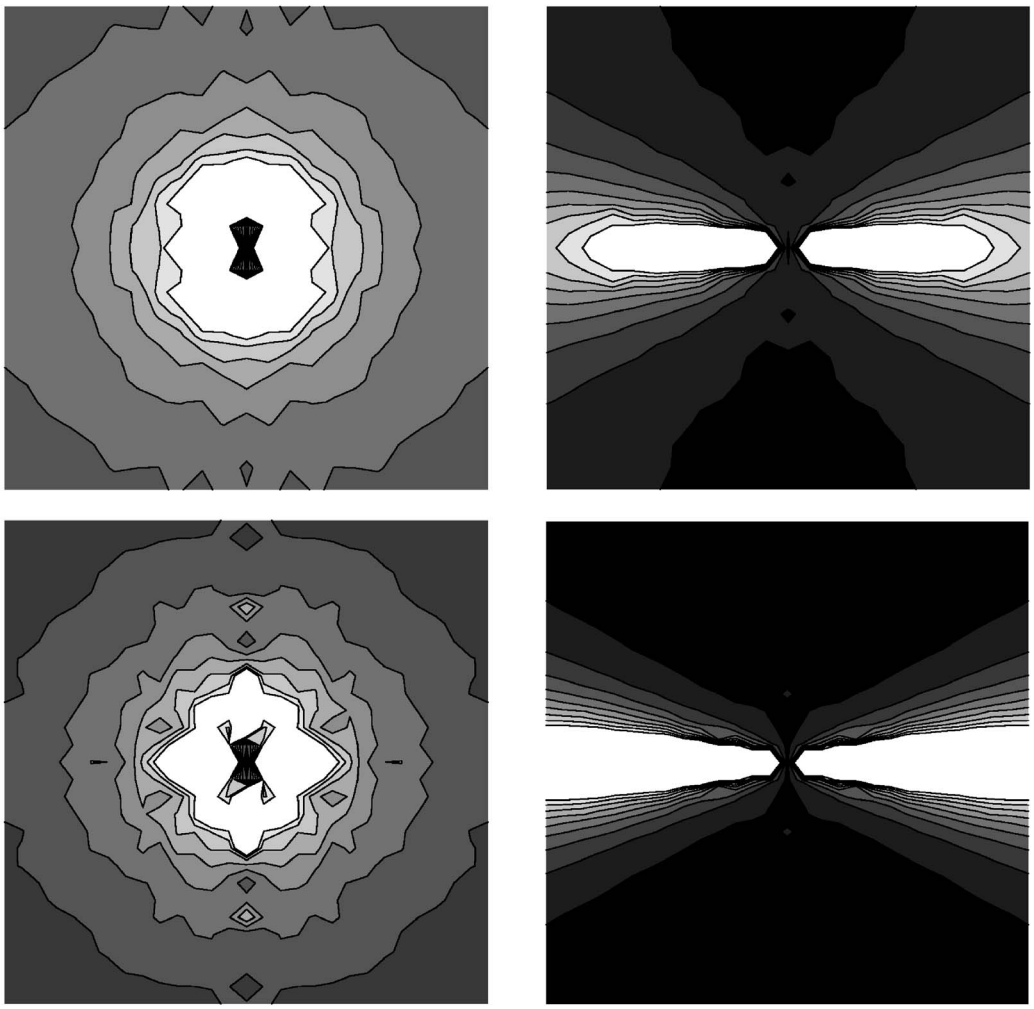

FIG. 6. *Monodispersed case*: 2D structure factor $S(q_\perp, q_\parallel)$ of monodispersed cases, with $-\pi \leqslant q_\perp \leqslant \pi$ and $-\pi \leqslant q_\parallel \leqslant \pi$, with an applied magnetic field perpendicular to the horizontal axis. From left to right panels: $\alpha = 0, 9$. From upper to lower panels: $\lambda = 4, 8$ (or $\rho = 0.075, 0.0375$). Bright (dark) regions indicate high (low) intensities.

smaller than 1 at low $q$. As $q$ increases, a peak is reached. Similar behavior can also be found in Fig. 5 in Ref. [27], where the sample A was investigated experimentally for various volume fraction $\phi$. Since the dipolar coupling constant $\lambda$ for the sample A was fixed at $\lambda = 1.75$, the frameworks for all the curves for various $\phi$ are similar as well. In Fig. 1, because of the different $\lambda$ in use, the framework can be changed significantly, especially at low $q$. This further demonstrates that the dipolar coupling constant $\lambda$ plays a crucial role in the formation of particle chains.

Figure 2 displays the ratio of the nonzero-field structure factor (at $\alpha = 9$) to the zero-field one as a function of $\lambda$, namely (a,b) $S(q_{xy})|_{\alpha=9}/S(q_{xy})|_{\alpha=0}$ and (c,d) $S(q_{xz})|_{\alpha=9}/S(q_{xz})|_{\alpha=0}$ for (a,c) $\chi_L = 0.4\pi$ and (b,d) $\chi_L = 1.6\pi$. Here the upper panels [namely (a) and (b)] stand for the ratio within the $XY$ plane, while the lower panels [namely (c) and (d)] denote the ratio within the $XZ$ plane. For the sake of clarity, we have omitted the curve for $\lambda = 1$ and $\rho = 0.3$ (this curve is similar to that for $\lambda = 4$ or 8). It is worth mentioning that due to symmetry, the result for the $YZ$ plane should be the same as that for the $XZ$ plane, as the external field is along the $z$ axis. From Fig. 2, it is found that all the structure factor ratio tends to be unit as the wave vector ($q_{xy}$ or $q_{xz}$) is large enough. In detail, for the $XY$ plane, high $\rho$ (or low $\lambda$) suppresses again the structure factor ratio at the region of low wave vectors $q_{xy}$. In contrast, as far as the $XZ$ plane is concerned, low $\rho$ (or high $\lambda$) suppresses the ratio at the corresponding region of low wave vectors $q_{xz}$. In addition, for the $XY$ plane, we find that the high field causes the structure factor to increase at the low $q_{xy}$ region, and hence the structure factor ratio is larger than unity, as shown in Figs. 2(a) and 2(b). This means the compressibility increases at high field values. Figure 8(b) in Ref. [27] (or Fig. 8 in Ref. [28]) shows the fact that for small $q$, the ratio of the $\theta = 90°$ structure factor at nonzero field to that at zero field should be larger than unity. This is also reflected in our Figs. 2(a) and 2(b), in which $S(q_{xy})|_{\alpha=9}/S(q_{xy})|_{\alpha=0}$ is displayed. However, for the $XZ$ plane, it is found that at high fields the $XZ$-plane structure factor is suppressed at low $q_{xz}$, and shows fewer fluctuations when compared to the data at high $q_{xz}$, see Figs. 2(c) and 2(d). Furthermore, we observe a clear peak in Figs. 2(c) and 2(d), located at $\sigma q_{xz} \approx 2\pi$, which corresponds to a real-space value $r \approx \sigma$. This means that the high field favors chain formation significantly. As mentioned in Sec. II C, ow-

ing to the isotropic behavior along the $x$ and $y$ axes, our $S(q_{xz})$ can be seen to be equivalent to the averaged structure factor $\bar{S}(\theta)$. For a certain $q$, the ratio of the averaged structure factor at nonzero field to that at zero field can be smaller or larger than unity, see Fig. 8 in Ref. [28] [or Fig. 8(b) in Ref. [27]]. This phenomenon has also been displayed in Figs. 2(c) and 2(d). In simple terms, the reason for the difference between the results obtained for the $XY$ and $XZ$ planes is due to the existence of anisotropy in the structure of our model ferrofluid.

In Fig. 3, we show the pair distribution functions (a,b) $g(r_{xy})$ and (c,d) $g(r_{xz})$ for (a,c) $\chi_L=0.4\pi$ and (b,d) $\chi_L=1.6\pi$ as a function of $\lambda$ at nonzero field ($\alpha=9$). As the external field is applied along the $z$ axis, chains start to form and get directed along the $z$ axis. Since the particle positions are projected onto the $XY$ plane, slight deviations from perfect alignment lead to a high probability for one particle to find another particle at $r_{xy}=0$. In this way, the shape and value of $g(r_{xy}=0)$ reflects the length and alignment of the chain into the $z$ direction. Thus, $g(r_{xy}) \gg 1$ as $r_{xy} \to 0$ [see Figs. 3(a) and 3(b)], which hints at the existence of the particle chains. The observed minimum at $\approx 2.5\sigma$ at $\lambda=8$ is probably due to the onset of a depletion zone due to the strong repulsion of the chains, analogous to a correlation hole in repulsively interacting systems. To see the depletion in real space observed for $\lambda=8$ in Fig. 3(a), we plot the projection of particle locations onto the $XY$ plane, see Fig. 4. There, the depletion zone can be clearly seen.

In detail, in Figs. 3(c) and 3(d) a series of peaks occur: (1) the higher height of a peak reflects both the formation of longer chains and the higher chain density (especially the density of short chains); (2) the higher the number of peaks is, the larger are the average particle chains. These two points are justified when comparing the cases with different $\lambda$ at a given $\chi_L$, see Figs. 3(c) and 3(d). In addition, since there are more peaks observed in the plots of $g(r_{xz})$ for $\alpha=9$ (nonzero field) than for zero field (no figure shown here), this also demonstrates that an external field increases the observed chain length, as can also be shown more directly in a real-space cluster analysis [25].

Finally, it is found that at a fixed value of $\lambda$, the number and peaks of $g(r_{xy})$ and $g(r_{xz})$ can be suppressed by higher densities, showing that chain formation is more difficult at higher densities [25,26]. In detail, at higher densities the enhanced angular correlation between the particles lets them distribute more uniformly, and thus there is less apparent long-range ordered chainlike structure in the system.

The structure factor in a given range of wave vectors can scale as [60]

$$S(q) \sim q^{-1/\nu}, \tag{19}$$

where $1/\nu$ is the fractal dimension ($1/\nu \leqslant 2$ in two dimensions and $1/\nu \leqslant 3$ in three dimensions), which characterizes the structure of a particle chain on a particular length scale. For rodlike molecules $\nu=1$, for a Gaussian chain $\nu=0.5$, and for a random self-avoiding walk in three dimensions $\nu=0.588$. Sufficiently long chains formed by strong dipolar interactions should behave similar to living polymers [21], and therefore we could expect some region of $q$ vectors where a corresponding scaling regime should be found.

Figure 5 shows the log-log plots of the structure factor for (a) $S(q_{xyz})$, which is the isotropic case, (b) $S(q_{xy})$, and (c) $S(q_{xz})$ for (a) zero field and (b,c) nonzero field. In these figures, the lines denote fits to the equation $S(q_{xyz})=Cq_{xyz}^{-1/\nu}$. At zero field ($\alpha=0$), $S(q_{xyz})$ was fitted in the range $1 \leqslant \sigma q_{xyz} \leqslant \pi$ [see Fig. 5(a)]. This choice of upper limit $\sigma q_{xyz}=\pi$ corresponds to a separation $\approx 2\sigma$. $S(q_{xyz})$ for $q_{xyz} > \pi$ is dominated by correlations between adjacent particles at or close to contact. We find $\nu=0.99$ for $\lambda=8$, $\rho\sigma^3=0.0375$, but a larger value of $\nu=1.74$ for $\lambda=8$, $\rho\sigma^3=0.15$. $\nu=0.99$ ($\sim 1$) denotes the rodlike behavior of the chain dominated system. However, in the more dense case of $\rho\sigma^3=0.15$, the value of $\nu$ increases to $\nu=1.74$. We have already seen that at higher densities the tendency to form chains is reduced, and it becomes more likely that rings can appear. A similar behavior was already seen in Ref. [22] and interpreted in this way. In this connection, it is worth mentioning that fitting $S(q_{xy})$ and $S(q_{xz})$ in the same range at zero field, the resulting values for $\nu$ are also roughly 0.99 and 1.74, respectively, which again demonstrates that the system is isotropic (figures not shown). The curve for $\lambda=4$ does not show any scaling behavior, since the chains are probably too small due to the smaller dipolar coupling.

At a large field value of $\alpha=9$, we investigated $S(q_{xy})$ and $S(q_{xz})$ in Figs. 5(b) and 5(c), respectively. $S(q_{xy})$ show a similar scaling behavior in the range $1 \leqslant \sigma q_{xy} \leqslant 2\pi$ as we have seen in Fig. 5(a), and was fitted to the same equation as before, see Fig. 5(b). This choice of upper limit $q_{xy}=2\pi$ is related to a separation $\approx\sigma$ for touching particles, however the sensitivity of the fit to the limits is rather strong. We find that $\nu=1.05$, 0.71, and 0.92 for $\lambda=4$ and $\rho\sigma^3=0.075$; $\lambda=8$ and $\rho\sigma^3=0.0375$; and $\lambda=8$ and $\rho\sigma^3=0.15$, respectively. Since the chains are now directed into the $z$ direction, it is not obvious how the projection of that into the $XY$ plane should scale. For $\lambda=8$ and $\rho=0.0375$, the peak in Fig. 3(a) at $r_{xy}=7.65$ is reflected as the first peak in Fig. 5(b) at $q_{xy} \approx 0.83$. Also the dips in the structure factor can be related to the occurrence of the correlation holes seen in Figs. 3(a) and 3(b).

The data for the three cases of $S(q_{xz})$ of Fig. 5(c) do not show any significant scaling behavior, except for the peak at real-space distances of $\approx\sigma$ for touching spheres, which does not contain any significant information.

Figure 6 shows the 2D structure factor pattern $S(q_\perp, q_\parallel)$ for monodispersed cases. The pattern is always isotropic at zero applied field, for different coupling constant $\lambda=4,8$. Only the application of an external applied magnetic field yields an anisotropic pattern. Then the structure factor becomes anisotropic with a significant increase of the strength perpendicular to the field axis, in contrast to a simultaneous decrease along the field axis. A similar behavior has also been found in the experimental SANS (small-angle neutron scattering) patterns of Ref. [27], see Figs. 3(a) and 8(a) therein. Our Fig. 6 further shows that larger $\lambda$ leads to a stronger degree of anisotropy, which is just indicative of particle chains of increasing length.

In Figs. 7–10 we investigate the bidispersed case of Ref. [26] in an attempt to study the influence of polydispersity in

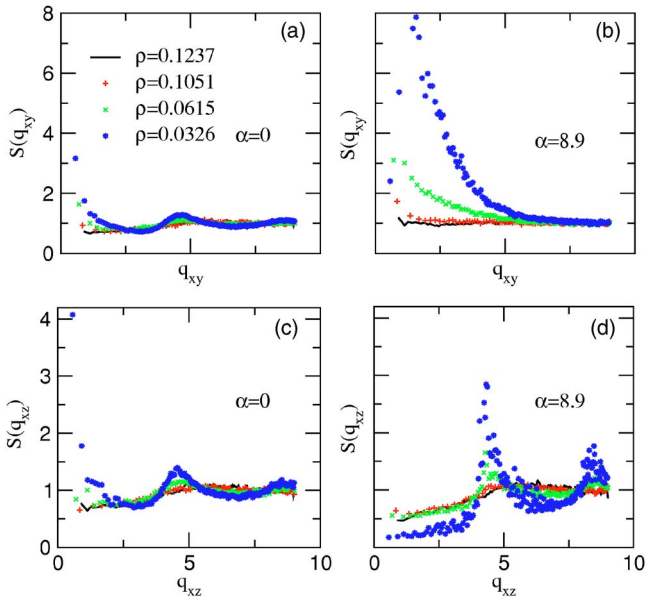


FIG. 7. (Color online) *Bidispersed case*: Structure factor (a,b) $S(q_{xy})$ and (c,d) $S(q_{xz})$ as a function of the volume fraction of large particles $\phi_L$, at (a,c) zero field and (b,d) nonzero field. The total volume fraction of the large and small particles is fixed to $\phi=0.07$. The number density $\rho=0.1237, 0.1051, 0.0615, 0.0326$ corresponds to the system of the volume fraction of the large particles $\phi_L=0.007, 0.02, 0.05, 0.07$, respectively.

the particle size and subsequently in the dipole moment. In the simulations, the total volume fraction $\phi$ of the large and small particles is fixed to $\phi=0.07$, and the volume fraction of the large particles is varied from 0.007 to 0.07 (only large particles present). Figure 7 shows the structure factor (a,b) $S(q_{xy})$ and (c,d) $S(q_{xz})$ as a function of the number density $\rho$ of all the particles (or the volume fraction of the large particles $\phi_L$), at (a,c) zero field and (b,d) nonzero field. In fact, at zero field ($\alpha=0$), the system under consideration behaves as an isotropic system, and hence Fig. 7(a) [$S(q_{xy})$] and Fig. 7(c) [$S(q_{xz})$] display the same behavior. In particular, at zero field or nonzero field, decreasing $\rho$ (i.e., increasing $\phi_L$) always causes $S(q_{xy})$ to increase in the low-$q_{xy}$ region [see Figs. 7(a) and 7(b)]. However, at nonzero field, decreasing $\rho$ causes $S(q_{xz})$ to decrease in the low-$q_{xz}$ region [see Fig. 7(d)]. Moreover, increasing the magnetic field leads to increasing $S(q_{xy})$ in the low-$q_{xy}$ region again, but decreasing $S(q_{xz})$ in the low-$q_{xz}$ region. In addition, it is found that $S(q_{xz})$ increases in the high-$q_{xz}$ region as the magnetic field increases. This is consistent with Fig. 2 in which a monodispersed case is studied. In Fig. 7(c) (zero field), a peak is induced to appear at about $q_{xz}=2\pi/\bar{r}$, where $\bar{r}\approx(\sigma_L+\sigma_S)/2$ for the bidispersed cases of $\rho=0.1237, 0.1051, 0.0615$ (namely, $\phi_L=0.007, 0.02, 0.05$) and $\bar{r}\approx\sigma_L$ for the monodispersed case of $\rho=0.0326$ (i.e., $\phi_L=0.07$). Similar behavior is found in Fig. 7(d) (nonzero field), in which, however, a clear second peak is observed. This second peak is located at $q_{xz}=4\pi/\bar{r}$, which is two times the location of the first peak. Note the peak value at nonzero field is much higher than that at zero field, which is also indicative of a larger presence of clusters in the system.

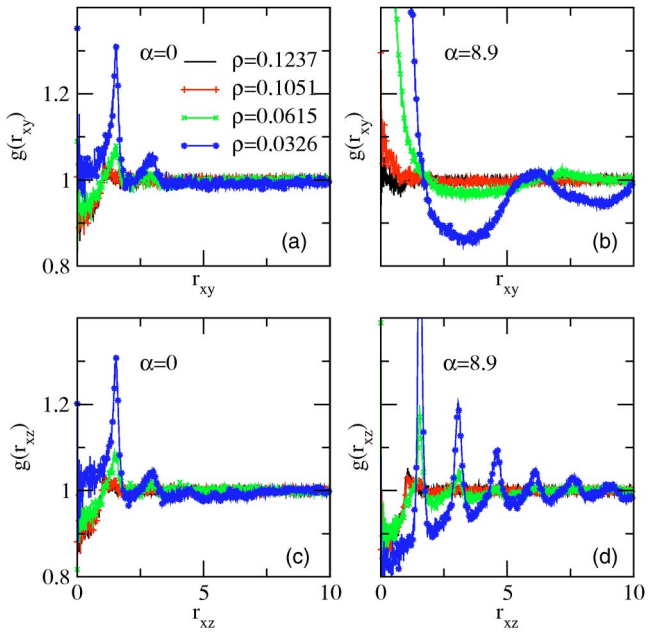


FIG. 8. (Color online) *Bidispersed case*: Same as Fig. 7, but for the pair distribution function (a,b) $g(r_{xy})$ and (c,d) $g(r_{xz})$.

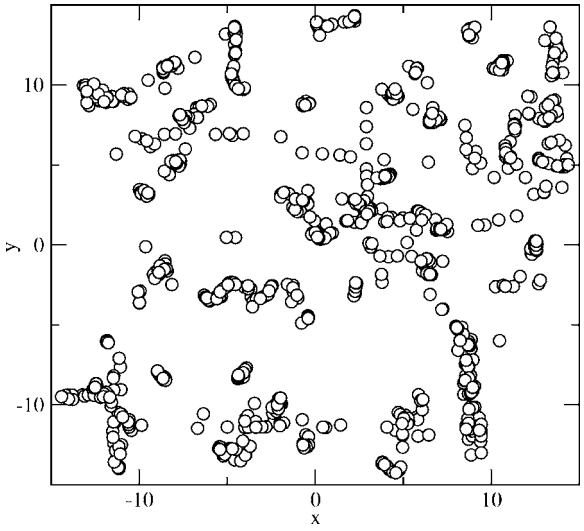


FIG. 9. Projection of particle locations onto the $XY$ plane, to account for the depletion observed for $\rho=0.0326$ (or $\phi_L=0.07$) in Fig. 8(b).

Similar to Fig. 7, Fig. 8 shows the anisotropic pair distribution function (a,b) $g(r_{xy})$ and (c,d) $g(r_{xz})$ at (a,c) zero field and (b,d) nonzero field. For the isotropic system, $g(r_{xy})$ [Fig. 8(a)] behaves the same as $g(r_{xz})$ [Fig. 8(c)] at zero field, since no anisotropy is present. In particular, for $\rho=0.0326$ (i.e., $\phi_L=0.07$), where only large particles are present, Figs. 8(b) and 8(d) shows a similar behavior to Fig. 3, where a monodispersed case is studied at nonzero field as well. At a high concentration of large interacting particles again a depletion zone due to repulsive dipolar interactions is seen for the case $\rho=0.0615$ and $\rho=0.0326$. To see the depletion in real space observed for $\rho=0.0326$ (or $\phi_L=0.07$) in Fig. 8(b), Fig. 9 is plotted to display the projection of particle locations

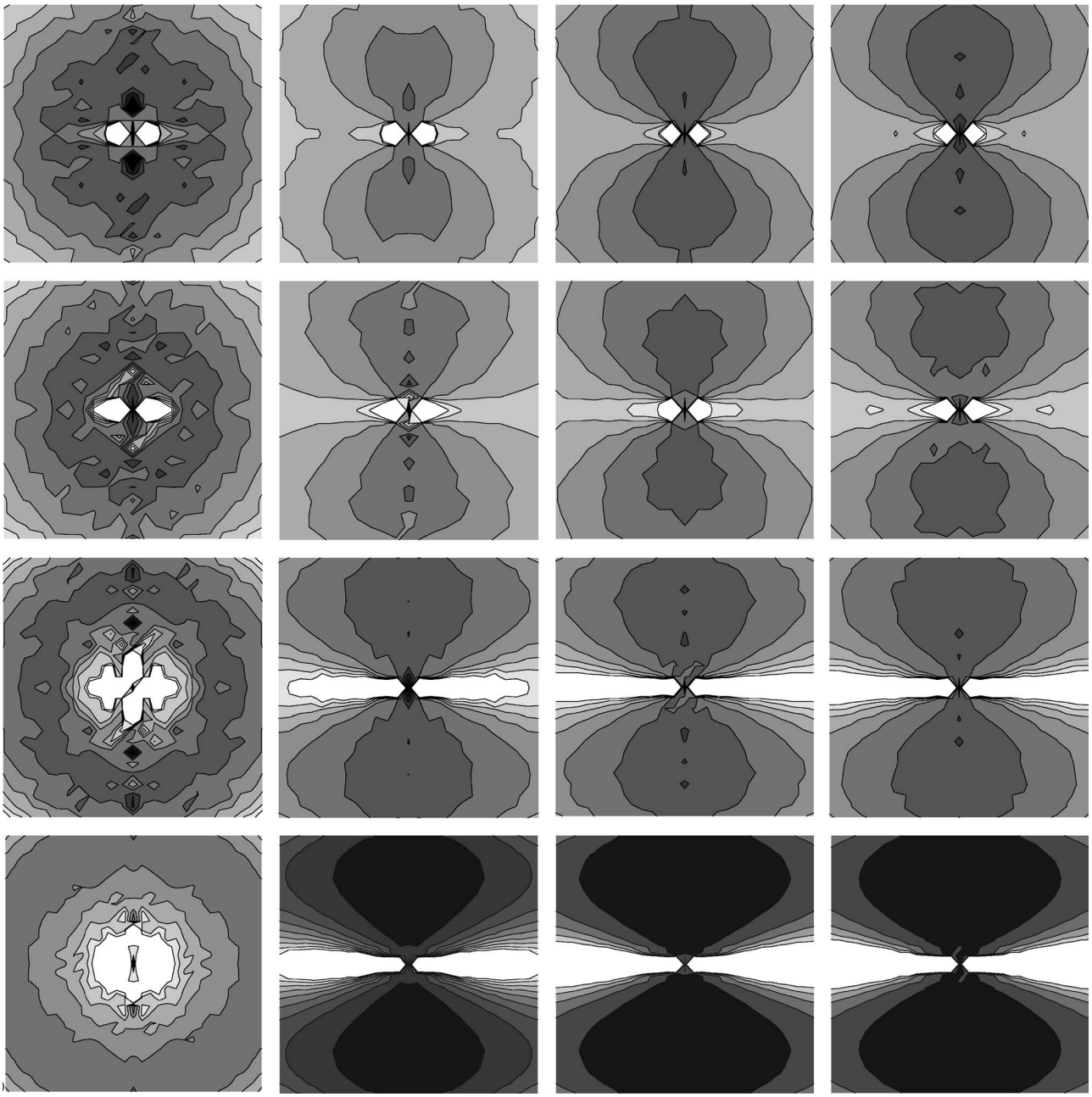

FIG. 10. *Bidispersed case*: 2D structure factor $S(q_\perp, q_\parallel)$ of bidispersed cases, with $-\pi \leqslant q_\perp \leqslant \pi$ and $-\pi \leqslant q_\parallel \leqslant \pi$, with an applied magnetic field perpendicular to the horizontal axis, at a fixed total volume fraction of both small and large particles $\phi = 0.07$. From left to right panels: $\alpha = 0, 2.9, 6.1, 8.9$. From top to bottom panels: volume fraction of large particles $\phi_L = 0.007, 0.02, 0.05, 0.07$.

onto the *XY* plane, where the depletion zone can be clearly observed.

In addition to what has been mentioned in Fig. 3, from Figs. 8(c) and 8(d) it can be nicely seen that, as $\rho$ decreases (or $\phi_L$ increases) and a large field is switched on, longer particle chains form inside the suspension, which is actually reflected by the higher number of peaks in these figures. In particular, clusters of size 6 are still visible, see Fig. 8(d). In other words, such chains exist for large particles only, which is due to their larger dipolar coupling constant compared to the small particles.

Similar to Fig. 6, in Fig. 10 we plot the 2D structure factor pattern $S(q_\perp, q_\parallel)$ for the bidispersed cases. The isotropic pattern obtained at zero field ($\alpha = 0$) becomes anisotropic for nonzero field ($\alpha \neq 0$). Moreover, the increase of magnetic field causes the degree of anisotropy to be increased. In the meantime, as the volume fraction of large particles increases, the degree of anisotropy can further be increased, because of the formation of more and more chains of the large particles. Due to numerical artifacts, the 2D structure factor patterns in Figs. 6 and 10 without magnetic fields are slightly anisotropic.

Regarding the bidispersed system, for the cases of the two smaller amounts of large particles, the obtained curves for structure factors and pair distribution functions seem to be identical within statistical error (Figs. 7 and 8). This can also

be shown in the 2D structure factor pattern in Fig. 10. So, the volume fraction of large particles $\phi_L$ should be large enough to show significant effect. In other words, in the present simulations, $\phi_L=0.05$ serves as a minimal concentration at which the effect of large particles is evident.

## IV. DISCUSSIONS AND CONCLUSIONS

In the limiting case of perfectly oriented dipoles [35,36], the ferrofluid particles are fully aligned, with negligible thermal fluctuations of the direction of magnetic moments. In this work, we have taken into account the thermal fluctuations of the direction of magnetic moments. As a matter of fact, the high-field system in this work just corresponds to the case of perfectly oriented dipoles discussed in Refs. [35,36], and particle chains can be found indeed as already predicted [35,36].

To summarize our work, we have used molecular-dynamics simulations to investigate the structure of the monodispersed and bidispersed ferrofluid, which was subjected to an applied magnetic field along the $z$ axis. The ferrofluid was modeled as a soft-sphere system having a purely repulsive LJ potential. In the simulations, we used the Ewald summation with metallic boundary conditions to treat the long-range dipolar interactions, and we took explicitly into account the translational and rotational degrees of freedom of the dipolar particles. The temperature was kept constant by means of a Langevin thermostat for all degrees of freedom. Our results for the isotropic structure factor are similar in trend to those obtained by using an alternative Monte Carlo method, although they were scanning a different parameter region close to an assumed critical region. In our work, we were mainly interested in the anisotropic structure factor and pair distribution functions, calculated for *XY* and *XZ* planes, respectively, in an attempt to investigate the anisotropy of the structure of our model ferrofluid. For this purpose, the 2D structure factor patterns $S(q_\perp, q_\parallel)$ were further investigated.

We have demonstrated that the analysis of structure factors as well as pair distribution functions can help to understand the formation of particle chains in ferrofluids. In fact, from the simulational point of view, based on the data of particle positions, we have already performed a cluster analysis [25,26] which gives an alternative proof for the presented results for the existence of particle chains. However, in view of the fact that in experiments structure factors rather than particle positions are measured directly, this paper is aimed at helping one to interpret experimental observations.

## ACKNOWLEDGMENTS

J.P.H. and C.H. acknowledge useful discussions with D. Antypov, P. Ilg, L. Pop, and S. Odenbach. J.P.H. thanks G. Mériguet and P. Turq for helpful comments on the anisotropic structure factors of ferrofluids. This work was supported by the DFG under Grant No. HO 1108/8-4, and by the Alexander von Humboldt Foundation in Germany (J.P.H.).

[1] B. M. Berkovsky, V. F. Medvedev, and M. S. Krakov, *Magnetic Fluids, Engineering Applications* (Oxford University Press, Oxford, 1993).
[2] C. Alexiou, W. Arnold, P. Hulin, R. Klein, A. Schmidt, C. Bergemann, and F. G. Parak, Magnetohydrodynamics **37**, 3 (2001).
[3] R. E. Rosensweig, *Ferrohydrodynamics* (Cambridge Univ. Press, Cambridge, 1985).
[4] C. F. Hayes, J. Colloid Interface Sci. **52**, 239 (1975).
[5] E. A. Peterson and D. A. Krueger, J. Colloid Interface Sci. **62**, 24 (1977).
[6] H. Mamiya, I. Nakatani, and T. Furubayashi, Phys. Rev. Lett. **84**, 6106 (2000).
[7] J. C. Bacri, R. Perzynski, D. Salin, V. Cabuil, and R. Massart, J. Colloid Interface Sci. **132**, 43 (1989).
[8] S. Odenbach and H. Gilly, J. Magn. Magn. Mater. **152**, 123 (1996).
[9] S. Odenbach and H. Störk, J. Magn. Magn. Mater. **183**, 188 (1998).
[10] S. Odenbach, *Magnetoviscous Effects in Ferrofluids, Lecture Notes in Physics* (Springer, Berlin, 2002).
[11] D. Wei and G. N. Patey, Phys. Rev. Lett. **68**, 2043 (1992).
[12] D. Wei and G. N. Patey, Phys. Rev. A **46**, 7783 (1992).
[13] J. J. Weis, D. Levesque, and G. J. Zarragoicoechea, Phys. Rev. Lett. **69**, 913 (1992).
[14] J. J. Weis and D. Levesque, Phys. Rev. E **48**, 3728 (1993).
[15] D. Levesque and J. J. Weis, Phys. Rev. E **49**, 5131 (1994).
[16] B. Groh and S. Dietrich, Phys. Rev. E **50**, 3814 (1994).
[17] G. Ayton, M. J. P. Gingras, and G. N. Patey, Phys. Rev. Lett. **75**, 2360 (1995).
[18] B. Groh and S. Dietrich, Phys. Rev. E **53**, 2509 (1996).
[19] J. J. Weis and D. Levesque, Phys. Rev. Lett. **71**, 2729 (1993).
[20] M. A. Osipov, P. I. C. Teixeira, and M. M. TelodaGama, Phys. Rev. E **54**, 2597 (1996).
[21] J. M. Tavares, J. J. Weis, and M. M. Telo da Gama, Phys. Rev. E **59**, 4388 (1999).
[22] P. J. Camp and G. N. Patey, Phys. Rev. E **62**, 5403 (2000).
[23] A. Y. Zubarev and L. Y. Iskakova, Phys. Rev. E **65**, 061406 (2002).
[24] L. Y. Iskakova and A. Y. Zubarev, Phys. Rev. E **66**, 041405 (2002).
[25] Z. Wang, C. Holm, and H. W. Müller, Phys. Rev. E **66**, 021405 (2002).
[26] Z. Wang and C. Holm, Phys. Rev. E **68**, 041401 (2003).
[27] F. Gazeau, E. Dubois, J.-C. Bacri, F. Boué, A. Cebers, and R. Perzynski, Phys. Rev. E **65**, 031403 (2002).
[28] G. Mériguet, M. Jardat, and P. Turq, J. Chem. Phys. **121**, 6078 (2004).
[29] R. W. Chantrell, A. Bradbury, J. Popplewell, and S. W. Charles, J. Appl. Phys. **53**, 2742 (1982).
[30] T. Tlusty and S. Safran, Science **290**, 1328 (2000).
[31] H. Morimoto and T. Maekawa, J. Phys. A **33**, 247 (2000).

[32] K. Butter, P. H. H. Bomans, P. M. Frederik, G. J. Vroege, and A. P. Philipse, Nat. Mater. **2**, 88 (2003).
[33] V. F. Puntes, K. M. Krishnan, and A. P. Alivisatos, Science **291**, 2115 (2001).
[34] Y. Lalatonne, J. Richardi, and M. P. Pileni, Nat. Mater. **3**, 121 (2004).
[35] J. B. Hayter and R. Pynn, Phys. Rev. Lett. **49**, 1103 (1982).
[36] S. Hess, B. J. Hayter, and R. Pynn, Mol. Phys. **53**, 1527 (1984).
[37] K. I. Morozov, A. F. Pshenichnikov, Y. L. Raikher, and M. I. Shliomis, J. Magn. Magn. Mater. **65**, 269 (1987).
[38] Y. A. Buyevich and A. O. Ivanov, Physica A **190**, 276 (1992).
[39] M. E. van Leeuwen and B. Smit, Phys. Rev. Lett. **71**, 3991 (1993).
[40] M. J. Stevens and G. S. Grest, Phys. Rev. Lett. **72**, 3686 (1994).
[41] M. J. Stevens and G. S. Grest, Phys. Rev. E **51**, 5962 (1995).
[42] M. J. Stevens and G. S. Grest, Phys. Rev. E **51**, 5976 (1995).
[43] A. Y. Zubarev and A. O. Ivanov, Phys. Rev. E **55**, 7192 (1997).
[44] P. J. Camp, J. C. Shelley, and G. N. Patey, Phys. Rev. Lett. **84**, 115 (2000).
[45] M. P. Allen and D. J. Tildesley, *Computer Simulation of Liquids*, 1st ed., Oxford Science Publications (Clarendon Press, Oxford, 1987).
[46] W. Loose and S. Hess, Rheol. Acta **28**, 91 (1989).
[47] L. Bennett, S. Hess, C. P. Borgmeyer, and T. Weider, Int. J. Thermophys. **19**, 1143 (1998).
[48] S. Hess, Int. J. Thermophys. **23**, 905 (2002).
[49] L. M. Pop, S. Odenbach, A. Wiedenmann, N. Matoussevitch, and H. Bönnemann, J. Magn. Magn. Mater. **289**, 303 (2005).
[50] M. I. Shliomis, Phys. Usp. **17**, 1876 (2000).
[51] A. O. Ivanov and O. B. Kuznetsova, Phys. Rev. E **64**, 041405 (2001).
[52] B. Huke and M. Lücke, Phys. Rev. E **67**, 051403 (2003).
[53] T. Kristóf and I. Szalai, Phys. Rev. E **68**, 041109 (2003).
[54] G. M. Range and S. H. L. Klapp, Phys. Rev. E **69**, 041201 (2004).
[55] Z. Wang, C. Holm, and H. W. Müller, J. Chem. Phys. **119**, 379 (2003).
[56] M. I. Shliomis, Usp. Fiz. Nauk **112**, 427 (1974).
[57] S. W. de Leeuw, J. W. Perram, and E. R. Smith, Proc. R. Soc. London, Ser. A **373**, 27 (1980).
[58] Z. Wang and C. Holm, J. Chem. Phys. **115**, 6351 (2001).
[59] J. P. Hansen and I. R. McDonald, *Theory of Simple Liquids* (Academic Press, London, 1986).
[60] P. M. Chaikin and T. C. Lubensky, *Principles of Condensed Matter Physics* (Cambridge University Press, Cambridge, 1995).